



## Full Text View

[Volume 28, Issue 5 \(May 1998\)](#)

### Journal of Physical Oceanography

Article: pp. 923–943 | [Abstract](#) | [PDF \(1.66M\)](#)

# Seasonal Cycles of Meridional Overturning and Heat Transport of the Indian Ocean

**Tong Lee**

*Jet Propulsion Laboratory, California Institute of Technology, Pasadena, California*

**Jochem Marotzke**

*Center for Global Change Science, Massachusetts Institute of Technology, Cambridge, Massachusetts*

(Manuscript received February 18, 1997, in final form September 2, 1997)

DOI: 10.1175/1520-0485(1998)028<0923:SCOMOA>2.0.CO;2

### ABSTRACT

A general circulation model of the Indian Ocean is fitted to monthly averaged climatological temperatures, salinities, and surface fluxes using the adjoint method. Interannual variability is minimized by penalizing the temporal drift from one seasonal cycle to another during a two-year integration. The resultant meridional overturning and heat transport display large seasonal variations, with maximum amplitudes of 18 and 22 ( $\times 10^6 \text{ m}^3 \text{ s}^{-1}$ ) for the overturning and 1.8 and 1.4 ( $\times 10^{15} \text{ W}$ ) for heat transport near 10°S and 10°N, respectively. A dynamical decomposition of the overturning and heat transport shows that the time-varying Ekman flow plus its barotropic compensation can explain a large part of the seasonal variations in overturning and heat transport. The maximum variations at 10°N and 10°S are associated with monsoon reversal over the northern Indian Ocean and changes of the easterlies over the southern Indian Ocean. An external mode with variable topography has a moderate contribution where the Somali Current and the corresponding gyre reverse direction seasonally. Contribution from vertical shear (thermal wind and ageostrophic shear) is dominant near the southern boundary and large near the Somali Current latitudes. The dominant balance in the zonally integrated heat budget is between heat storage change and heat transport convergence except south of 15°S.

Optimization with seasonal forcings improves estimates of sea surface temperatures, but the annual average overturning and heat transport are very similar to previous results with annual mean forcings. The annual average heat transport consists of roughly equal contributions from time-mean and

#### Table of Contents:

- [Introduction](#)
- [Data and model](#)
- [Hydrography-only experiment](#)
- [Inclusion of TOPEX data](#)
- [Concluding remarks](#)
- [REFERENCES](#)
- [TABLES](#)
- [FIGURES](#)

#### Options:

- [Create Reference](#)
- [Email this Article](#)
- [Add to MyArchive](#)
- [Search AMS Glossary](#)

#### Search CrossRef for:

- [Articles Citing This Article](#)

#### Search Google Scholar for:

- [Tong Lee](#)
- [Jochem Marotzke](#)

time-varying fields of meridional velocities and temperatures in the northern Indian Ocean, indicating a significant rectification to the heat transport due to the time-varying fields. The time-mean and time-varying contributions are primarily due to the overturning and horizontal gyre, respectively.

Inclusion of TOPEX data enhances the seasonal cycles of the estimated overturning and heat transport in the central Indian Ocean significantly and improves the estimated equatorial zonal flows but leads to unrealistic estimates of the velocity structure near the Indonesian Throughflow region, most likely owing to the deficiencies in the lateral boundary conditions.

## 1. Introduction

The surface circulation of the northern and equatorial Indian Ocean displays the largest seasonal variations in the World Ocean due to the seasonal reversal of the monsoon. Major characteristics of the seasonal surface circulation are relatively well known, for example, the reversal of the near-surface portion of the Somali Current ([Schott et al. 1990](#)) and the semiannual equatorial jet ([Wyrki 1973](#)). The overall variability of the subsurface circulation and the underlying mechanisms are much less certain. As a result, seasonal oceanic heat transport and the related physical processes are not well understood, making it difficult to assess the role of the Indian Ocean in the heat budgets of the Southern Hemisphere and the monsoon system.

Observations have furthered the knowledge about temporal variability of subsurface flow in limited areas such as the Somali Current region ([Schott et al. 1989, 1990](#)) and the Indonesian Throughflow area ([Fieux et al. 1996](#); [Meyers 1996](#)). Much of the understanding of the overall variability of surface as well as subsurface circulation has come from modeling studies. Layer models (e.g., [McCreary et al. 1993](#)) reproduced much of the observed variability for the upper few hundred meters of the Indian Ocean. However, variability of the deeper circulation must be investigated using general circulation models (GCMs).

The GCM simulations by [Latif et al. \(1994\)](#) and [Anderson and Carrington \(1993\)](#) focused on the near-surface circulation. [Semtner and Chervin \(1992\)](#) commented on the weak deep inflow into the Indian Ocean in their global GCM, but did not investigate the circulation in detail. Only recently did [Wacongne and Pacanowski \(1996\)](#) and [Gartnrecht and Schott \(1997](#), manuscript submitted to *J. Geophys. Res.*, hereafter GS97), by analyzing a high-resolution regional and global GCM respectively, explicitly examine the meridional overturning and heat transport of the Indian Ocean. The former one, confined to the area north of 15°S, assumed the absence of property exchanges between the Indian and Pacific Oceans, while the latter included the Indonesian Throughflow. Large seasonal variations in meridional overturning and heat transport were found in both cases. However, neither study examined the consistency of the solution with subsurface hydrographic data. To date, the only GCM inversion of Indian Ocean hydrography was performed by [Lee and Marotzke \(1997](#), LM hereafter) with annual mean data and forcings.

This paper is an extension of the annual mean inversion of LM, where a side-boundary condition estimation procedure is used to obtain an annual mean solution of the GCM that is in overall consistency with climatological data. The resultant dominant meridional overturning is shallow (<1000 m), is primarily driven by wind, and is the major carrier of heat toward the south. This study expands the scope of that preceding effort by introducing seasonal data and forcings in the inversion. The goal is to infer the seasonal cycle of the meridional overturning circulation and heat transport of the Indian Ocean by fitting the dynamics of a GCM to seasonal data. Specific objectives are 1) to assess the effect of seasonal forcings on annual mean estimates of the Indian Ocean circulation and thermal structure, 2) to examine the strength and structure of seasonal variations in meridional overturning and heat transport, and 3) to highlight dominant mechanism(s) controlling these variations. The effort also serves to develop a framework for synthesizing in situ data collected during the World Ocean Circulation Experiment (WOCE) Indian Ocean Expedition and satellite data (e.g., TOPEX) with the full dynamics of a GCM.

In [section 2](#), the data, the model, and the method used for the synthesis are described. [Section 3](#) focuses on the estimated meridional overturning and heat transport as well as a dynamical decomposition of seasonal anomalies of the meridional streamfunction and heat transport to highlight the relative contributions of different mechanisms; rectification due to seasonal forcings is also discussed; our results are compared with other studies. These are followed by results from a combined hydrography–altimetry data assimilation experiment ([section 4](#)). The findings are summarized in [section 5](#).

## 2. Data and model

Three types of data are used in this study: 1) Climatological monthly mean temperatures and salinities ([Levitus and Boyer 1994](#); [Levitus et al. 1994](#)). This dataset will be referred to as the Levitus data hereafter. In situ temperatures are converted to potential temperatures, which will be denoted by  $T$  throughout the paper. 2) Gridded ( $2^\circ \times 2^\circ$ ) anomalies of sea surface height derived from the TOPEX/Poseidon altimeter for the period of 1993–95, referenced to the time mean of this period.

Monthly averages are computed from the original data, which have a 10-day sampling interval. A Laplacian filter is applied to reduce small-scale variabilities. After interpolating to the model grid, surface geostrophic velocity anomalies are computed from the height anomalies except for the region within  $\pm 2.5^\circ$  of the equator where geostrophy is not a good assumption. 3) Climatological surface fluxes, which include the monthly means of wind stress (Hellerman and Rosenstein 1983) and surface heat and freshwater fluxes (Oberhuber 1988).

The assumed errors for temperatures and salinities (Table 1) are the same as those used by LM in the annual mean case except that the errors are reduced by approximately 50% in the upper 250 m (and tapered down toward deeper levels) in order to exclude the contribution of seasonal cycle to annual mean data error (variability due to the seasonal cycle is treated as “error” in the annual mean inversion). The errors of the geostrophic velocities are chosen to be the submonthly variability (i.e., variation within three consecutive cycles being 10 days apart) averaged over different longitudes. They are presented as a function of latitude in Fig. 1. In analyzing the TOPEX data, we found that the contribution of interannual variability is as large as the submonthly variability (especially near the Indonesian Throughflow area). Such a large interannual variability is not included in the a priori errors for reasons that will become clear later on.

The GCM used is the GFDL primitive equation model (Cox 1984). The horizontal resolution is  $1.5^\circ \times 1.5^\circ$ . There are 24 vertical levels with the interval between two adjacent levels ranging from 25 m near the surface to 500 m near the bottom. The domain is the Indian Ocean north of  $32^\circ\text{S}$ . Sponge layers are used near connections to the Antarctic Circumpolar Current, the Indonesian Throughflow, the Red Sea, and the Persian Gulf to simulate baroclinic exchanges of mass, heat, and salt between the model interior and the neighboring basins. The adjoint to the GFDL model is the same as that of LM except that it is modified to accommodate seasonal hydrography and altimetry data as well as seasonal surface and side-boundary forcing estimation. The history of development of the prototype adjoint code was described in LM.

During the assimilation experiments, the forward model is integrated for two years. In the first experiment in which temperatures, salinities, and surface fluxes are assimilated, a quadratic cost function  $J$  is used to penalize the interannual variability (first term) and model–data misfit (second term) of  $T$  and  $S$  in the model interior, deviations of estimated target  $T$  and  $S$  in sponge layers from climatological values (the third term), and deviations of estimated surface forcings from climatological values (the fourth term):

$$\begin{aligned}
 J = & \sum_{m=1}^{12} (\mathbf{x}^m - \mathbf{x}^{m+12})^T \mathbf{W}_s (\mathbf{x}^m - \mathbf{x}^{m+12}) \\
 & + \sum_{m=13}^{24} (\mathbf{x}^m - \mathbf{x}_d^m)^T \mathbf{W}_d (\mathbf{x}^m - \mathbf{x}_d^m) \\
 & + \sum_{m=13}^{24} (\mathbf{x}_{sp}^m - \mathbf{x}_{sp_d}^m)^T \mathbf{W}_{sp_d} (\mathbf{x}_{sp}^m - \mathbf{x}_{sp_d}^m) \\
 & + \sum_{m=13}^{24} (\mathbf{f}^m - \mathbf{f}_d^m)^T \mathbf{W}_f (\mathbf{f}^m - \mathbf{f}_d^m),
 \end{aligned}$$

where  $\mathbf{x}$  and  $\mathbf{x}_d$  are estimated and observed  $T/S$  in model interior;  $\mathbf{x}_{sp}$  and  $\mathbf{x}_{sp_d}$  are estimated and prior  $T/S$  in sponge layers;  $\mathbf{f}$  and  $\mathbf{f}_d$  are estimated and prior surface forcings. The elements of the vectors correspond to  $T$  and  $S$  at different grid points. Each  $\mathbf{W}$  is a weight matrix taken as the inverse of the a priori observational error covariance (subscripts “ $s$ ” and “ $d$ ” stand for steadiness and data and “ $sp$ ” stands for sponge layer). Following Marotzke (1992) and LM,  $\mathbf{W}_s$  is chosen to be  $100 \times \mathbf{W}_d$ . In this context it implies that the penalty to interannual variability is 10 times as strong as the penalty for model–data misfit during the 2-yr integration. Apart from strong constraints imposed by the forward model equations, two extra strong constraints are imposed to ensure that the estimated target  $T/S$  in sponge layers and estimated surface forcings for the same month of two different years are identical:  $\mathbf{x}_{sp}^m = \mathbf{x}_{sp}^{m+12}$ ,  $\mathbf{f}^m = \mathbf{f}^{m+12}$ . The estimation of sponge layer properties reflected by the third term in  $J$  marks a major difference from the conventional sponge layer treatment in regional modeling where the model properties (e.g.,  $T$  and  $S$ ) are simply relaxed toward fixed target values either taken from climatology or from a hydrographic section.

LM discussed the role of sponge layers on simulation and assimilation in section 5c of their paper. The key findings are summarized in the following. The solution of a forward simulation is sensitive to the prescribed target values of temperatures and salinities in sponge layers and to the relaxation constant. However, it is this sensitivity that allows one to inversely

estimate the target values using interior data and model dynamics. The optimized solution is not sensitive to the choice of prior target values: the optimized solutions using prior target values of temperatures and salinities obtained from the 1982 Levitus climatology (Levitus 1982), the 1994 version of the climatology (Levitus and Boyer 1994; Levitus et al. 1994), and the hydrographic section near 32°S (Toole and Warren 1993) mapped to the model grid are all very similar. The optimized solution is not sensitive to the choice of the relaxation constant either: a smaller relaxation constant is compensated by sharper estimated zonal gradients of temperature and salinity and vice versa, resulting in a similar amount of heat and salt exchanges between the model interior and sponge layers (which are determined by data constraints in the model interior rather than by prior target values in sponge layers). It remains to be seen how the solution obtained from this crude formulation of open boundary estimation would be different from that obtained from a formal open boundary estimation.

In the second experiment, altimetry data (TOPEX) are included in the assimilation as additional constraints. An extra term is included in  $J$  to penalize the deviations of anomalies of the monthly averaged model velocities at the second level (37.5 m),  $\mathbf{v}$ , from TOPEX-derived surface geostrophic velocity anomalies,  $\mathbf{v}_{tp}$ :  $\sum_{m=1}^{24} (\mathbf{v}^m - \mathbf{v}_{tp}^m)^T \mathbf{W}_{tp} (\mathbf{v}^m - \mathbf{v}_{tp}^m)$ . We chose to penalize the second-level model velocities because the first level (25 m thick) is influenced by Ekman velocities that are not measured by TOPEX.

The cost function  $J$  is minimized by optimally adjusting the control variables, which are initial  $T$  and  $S$ , monthly sponge-layer target  $T$  and  $S$ , and monthly surface fluxes, provided that model dynamics are fulfilled. In other words, optimal sets of initial and boundary conditions are sought subject to the strong constraints of model dynamics. The adjoint method converts such a constrained minimization problem into an unconstrained one by introducing Lagrange multipliers, which are solutions of the adjoint (of the forward model) integrating backward in time. Lagrange multipliers transmit penalty information back to the initial time (i.e., the end of the adjoint) and provide gradients of the cost function  $J$  with respect to the control variables. These gradients are used in a conjugate gradient algorithm to correct the control variables to reduce  $J$ . The procedure is then iterated until  $J$  decreases down to a statistically acceptable threshold and levels out. Detailed descriptions of the adjoint formulation can be found, for example, in Thacker and Long (1988).

### 3. Hydrography-only experiment

The GCM is integrated forward for 100 years, initialized from Levitus climatology and forced by climatological surface fluxes and relaxation to Levitus data in sponge layers. It reaches a quasi-equilibrium state in a relatively short time (less than 10 yr). The meridional transport streamfunction for January and July, the peak of the northeast and southwest Monsoon seasons, are shown in Figs. 2a and 2b. The meridional overturning changes dramatically from one monsoon season to the other. The 12-month averaged streamfunction (Fig. 2c) is very similar to that using annual mean forcings, which is a wrong overturning caused by biased zonal density gradients in southern sponge forcing unrealistic inflow/outflow between this sponge and the model interior (LM). The inclusion of seasonal surface and side-boundary forcings does not correct this problem.

The optimization experiment is initialized from the January state after one year of forward integration. The 100-yr integration is not used because the interior has drifted quite far away from Levitus data. After 80 iterations of minimization, the cost function decreases to a level well below the overall consistency threshold (defined as the cost value that results when every constraint is fulfilled to within one standard deviation) and almost levels out (Fig. 3).

The prior and estimated wind stresses and their differences (estimated – prior) are shown in Fig. 4. The estimated wind is not as smooth as the prior. Along the Indonesian coast and near the equator, the estimated zonal wind stresses are more eastward than the prior. The opposite is true for the region between 4°N and 10°N. These differences are better illustrated in the zonally averaged zonal wind stress (Fig. 5), which indicates an enhancement of the intertropical convergence zone in the estimated wind. To verify this, a comparison is made between the prior and estimated wind stress curls. The ITCZ, which is evident from the zero-curl line between the equator and 10°N, indeed shows up much clearer in the estimated wind stress curl (figure not shown). The zonally averaged estimated zonal wind stress differs from the prior by approximately 0.4 and –0.3 dyn cm<sup>-2</sup> at 1°N and 7°N in January (Fig. 5), which are smaller than the a priori error of 0.5 dyn cm<sup>-2</sup>. No systematic difference over all latitudes is found. Only 5.2% and 3.3% of the estimated zonal and meridional wind stresses in January deviate from their prior estimates by more than the a priori error. The percentages for July are even smaller (1.9% and 0.9%, respectively). Therefore, the estimated wind stresses are overall consistent with the prior estimates.

Overall speaking, the estimated  $T$  and  $S$  fields are consistent with Levitus data. All results presented in the following are taken from the second year of the optimized 2-yr model history. The distribution of model–data misfit with time is relatively uniform. Although the 12-month averaged model–data misfit and temporal drift are overall similar to those resulting from the annual mean experiment performed by LM, the estimated SST with seasonal forcings are closer to Levitus data than those with annual mean forcings in the northern Indian Ocean (Fig. 6), indicating an improved inversion when the seasonal cycle is included. This has an important consequence to the estimated meridional heat transport discussed later on.



The estimated surface circulations for January, April, July, and October are shown in [Figs. 7a–d](#) (square roots of the velocities are plotted to reduce the contrast of very large and very small vectors). Except near coastal boundaries and the equator, the surface current pattern bears a resemblance to that of the theoretically calculated Ekman flow. The estimated currents reproduce most well-known large-scale features such as the reversal of the surface Somali Current off the African coast ([Schott et al. 1990](#)) and the Monsoon Current south of Sri Lanka ([Schott et al. 1994](#)) ([Figs. 7a and 7c](#)), the semiannual equatorial jet during transition periods between the two monsoons ([Figs. 7b and 7d](#)) ([Wyrtki 1973](#)); the North Equatorial Current and the Equatorial Countercurrent during the northeast monsoon ([Fig. 7a](#)), and the South Equatorial Current that persists throughout the year compare reasonably well with ship drift data and regional model simulations presented by [McCreary et al. \(1993\)](#) and [Wacongne and Pacanowski \(1996\)](#), and with the Indian Ocean section of the global GCM presented by GS97 ([Fig. 3](#), [Fig. 2e](#), and [Fig. 2](#) in these three papers, respectively). The Great Whirl cannot be resolved in our study due to the low resolution. The width of the model Agulhas Current is too large and is not well developed within the model domain partly because the southern boundary is not far enough to the south and partly due to the low resolution of the model.

The external mode streamfunctions for January and July ([Figs. 8a and 8b](#)) show the dramatic seasonal changes, especially in the northern Indian Ocean where the gyre reverses its direction. The maximum variation in the strength of the gyre,  $-18$  Sv (January) to  $38$  Sv (July), occurs near  $6^\circ\text{N}$  due to the Somali Current reversal ([Figs. 8c and 8d](#)). The vertical structure associated with the reversal of the Somali Current is latitude dependent. From  $4^\circ$  to  $6^\circ\text{N}$ , the reversal from January to July is almost over the whole water column, as illustrated by the meridional velocity section at  $5.75^\circ\text{N}$  ([Figs. 9a and 9b](#)). From  $4^\circ\text{S}$  to  $3^\circ\text{N}$ , however, the reversal occurs in a surface layer  $50$ – $120$  m thick and below  $400$ – $700$  m, but not in between. An example is shown in [Figs. 9c and 9d](#) (at  $0.25^\circ\text{S}$ ). This multimodal behavior of the Somali Current reversal near the equator is consistent with the model result of [Wacongne and Pacanowski \(1996\)](#), and with current measurements by [Schott et al. \(1990\)](#) from October 1984 to October 1986. The magnitude of deep flow reversal in the model is however much weaker than that observed by [Schott et al. \(1990\)](#),  $7$ – $10$   $\text{cm s}^{-1}$ , during that 2-yr period. Note that hydrographic measurements made at the same region by [Warren and Johnson \(1992\)](#) during the winter of 1986/87 and the summer of 1987, a year of weak monsoon, do not suggest the deep flow reversal.

The response of the modeled Somali Current system within a few degrees of the equator to monsoon reversal compares reasonably well with the observational synopsis by [Schott et al. \(1990\)](#), schematically presented in their [Fig. 9](#). Moreover, our estimated flow field in January indicates that the southwestward flowing surface layer becomes thicker ( $50$  to  $120$  m), from  $4^\circ\text{S}$  to  $3^\circ\text{N}$ , while the northeastward flowing intermediate layer gets thinner (from  $700$  to  $400$  m); this intermediate layer converges with the southwestward flowing waters from the north between  $3^\circ$  and  $4^\circ\text{N}$ .

[Leetmaa and Stommel \(1980\)](#) investigated zonal currents above the thermocline near  $55^\circ\text{E}$  and within a few degrees of the equator based on hydrographic sections occupied during February–June of 1975 and 1976. They found a well-defined eastward Equatorial Undercurrent (EUC) between the equator and  $2^\circ\text{S}$  and centered at  $50$ – $100$  m throughout the measurement period; the EUC shifts southward to merge with the eastward Equatorial Countercurrent (ECC) farther south during May and June. In our hydrography-only experiment, the EUC appears in January and merges with the ECC in February. Only after TOPEX data is assimilated (as will be discussed in [section 5](#)) does the EUC become much closer to their observations in magnitude and phase.

From moored records in the western equatorial upper Indian Ocean ( $47^\circ$ – $62^\circ\text{E}$  and  $200$ – $750$  m), [Luyten and Roemmich \(1982\)](#) found that the zonal velocity for that region is dominated by a semiannual period. Our estimated zonal velocity field for the same region (figure not shown) compares favorably with the observations: it displays a dominant semiannual period with maximum westward (eastward) flow during June and November (February and September). This oscillation in the model is, again, several times weaker than that of the observations.

The limited ability of the model in reproducing these equatorial zonal currents is caused by many factors including the low horizontal and vertical resolution, crude formulation of mixing, and smoothness of the climatological data used. While these equatorial zonal flows may be coupled to local meridional flows near the equator, it is not obvious how they affect the overall meridional overturning and heat transport, which are foci of this paper. Further discussion of the zonal velocity field is thus beyond the scope of this paper.

### *a. Meridional overturning*

The estimated meridional transport streamfunctions for January and July as well as their corresponding seasonal anomalies (i.e., with 12-month average removed) are shown in [Fig. 10](#). The variations are large in magnitude as well as in spatial extent. The maximum change in overturning strength, approximately  $\pm 20$  Sv ( $\text{Sv} \equiv 10^6 \text{ m}^3 \text{ s}^{-1}$ ) occurs near  $10^\circ\text{S}$  and  $10^\circ\text{N}$ , corresponding to the latitudes having the largest seasonal variation in zonal wind stress. The overturning anomaly shows the reversal is coherent over most latitudes and almost over the whole water column.

In previous studies, interpretations of meridional transport streamfunctions are mostly qualitative. It is often very difficult to explain the detailed structure of the streamfunction because 1) the streamfunction is a zonally averaged picture that merges many zonally varying features, including zonally variable topography, and 2) the streamfunction is an abstract representation of all physical mechanisms that affect the meridional circulation. In this study, we attempt to decompose the meridional streamfunction into various dynamical components to evaluate the relative contributions of different physical processes.



First, the meridional velocity  $\mathbf{v}(x, y, z)$  is locally decomposed into three dynamical components:




$$\begin{aligned} \mathbf{v}(x, y, z) = & \frac{1}{H} \int_{-H}^0 \mathbf{v}(x, y, z) dz \\ & + \left[ \mathbf{v}_e(x, y, z) - \frac{1}{H} \int_{-H}^0 \mathbf{v}_e(x, y, z) dz \right] \\ & + \mathbf{v}_{sh}(x, y, z) \end{aligned} \quad (1)$$

(where  $H$  is a function of  $x$  and  $y$ ). The first component is the depth-averaged meridional flow. It describes the external mode (or barotropic gyre circulation) that is governed by the barotropic vorticity equation, a generalized Sverdrup relation with time dependence, bottom topography, and frictional effects (important near the western boundary). The external mode influences the meridional overturning in the presence of zonally nonuniform topography. One could envision this effect through two examples: 1) when a western boundary current travels northward along a coast having a depth of 1000 m and the return flows go southward over much greater depths, the zonal integration will result in an overturning characterized by a net northward flow above 1000 m and southward flow below it; 2) the zonal component of a horizontal barotropic gyre going over zonally nonuniform topography will cause net upwelling or downwelling upon zonal integration. These two examples would help understand the detailed structures in the overturning caused by the external mode presented later on.

The second component in [Eq. \(1\)](#) is the Ekman flow minus its vertical average, that is, minus its projection onto the external mode (note that the vertical average of  $\mathbf{v}_e$  has been included in the external mode). This component therefore represents the surface Ekman flow and its barotropic compensation beneath the surface. The Ekman velocity  $\mathbf{v}_e$  is calculated from the theoretical relation  $\tau_x/(f\rho_0)$ . The third component represents vertical shear consisting largely of thermal wind shear balanced by zonal density gradients (except near the equator) and small ageostrophic shear associated with friction and nonlinear effects. Note that this component also sums up to zero over depth because its depth average has been included in the external mode.

By integrating separately the three terms in 1) zonally and vertically, the corresponding contributions to the meridional overturning are obtained. For a flat-bottomed ocean, zonal integration of the thermal wind shear is simply proportional to the density difference between the eastern and western boundaries, making this density difference a useful diagnostic quantity ([Marotzke 1997](#)). In the presence of topography, however, it is difficult to separate thermal wind and ageostrophic shear contributions in section integrations because the integral is coupled to the bottom pressure difference at any given depth. We therefore do not present a further analytical breakdown of the vertical shear component of the overturning into thermal wind and ageostrophic contributions.

The decomposition is performed on the annual average overturning, total seasonal overturning, and seasonal anomaly of the overturning, and well characterizes the dominant process for the seasonal cycle of the overturning. As an example, the decomposition of the January overturning anomaly is shown in [Fig. 11](#) . Within a few degrees of the equator, large cancellation is found between the vertical shear and the ‘‘Ekman’’ components. This indicates that the decomposition is not meaningful there because the ‘‘Ekman’’ flow is ill-defined and the surface flow is not compensated by a barotropic return flow. Therefore, this region is masked out in [Figs. 11c and 11d](#) .

North of 25°S and away from the equator, the Ekman component ([Fig. 11c](#) ) explains a large part of seasonal variation in the total streamfunction anomaly ([Fig. 11a](#) ): it is dominated by two Ekman cells centered near 10°S and 10°N with strengths of 18 and 30 Sv. The northern cell, being stronger, is associated with Monsoon reversal over the northern Indian Ocean. The weaker southern cell is associated with the changes in the strength and the latitude of easterlies over the southern Indian Ocean. The strength of the southern Ekman cell is the same as that of the southern cell in the total overturning anomaly. However, the structure is different in that the center of the Ekman cell is near the surface (below the Ekman layer) and the latter is at a depth of about 800 m (near 12°S). This subsurface cell in the total overturning anomaly is contributed by the external mode and vertical shear ([Figs. 11b and 11c](#) ). For the northern Indian Ocean, there are two similarities between the total anomaly and the Ekman component: 1) they are both centered near the surface; 2) the lower

part, the 2- and 6-Sv streamlines, resembles each other. However, the cell enclosed by the 10-Sv streamline is weaker and shallower in the total anomaly than in the Ekman component. The difference in strength is caused by the fact that the southward transport in the first layer is smaller than the Ekman transport (22 as opposed to 30 Sv). To investigate this difference, the surface meridional velocity anomaly in the first layer is compared with the Ekman velocity anomaly. Off the Somali coast (in July), the surface flow is northward, opposing the meridional Ekman transport (not shown). This results in a smaller zonally integrated southward flow at the surface layer than the Ekman flow. The difference in structure (i.e., penetration depth) is due to the large vertical shear associated with the Somali Current, as shown in [Fig. 11d](#) between  $5^{\circ}$  and  $8^{\circ}\text{N}$ , which opposes the Ekman cell.

The change in overturning strength due to the external mode ([Fig. 11b](#)) is primarily associated with the reversal of the Somali Current and its corresponding gyre and results in a moderate overturning north of  $10^{\circ}\text{S}$ . In January, the overturning north of  $10^{\circ}\text{S}$  is generally anticlockwise with 1) moderate downwelling between  $10^{\circ}\text{S}$  and the equator primarily due to the zonal flow from the shallow African coast into the Somali basin and 2) moderate upwelling north of  $10^{\circ}\text{N}$  due to the flow from the Arabian Basin onto the African coast (see [Fig. 8c](#)). There are two small anticlockwise cells centered near the equator and  $10^{\circ}\text{N}$ , having strengths of 6 and 8 Sv. They are separated at  $5^{\circ}\text{N}$  by upwelling between the equator and  $5^{\circ}\text{N}$  and downwelling between  $5^{\circ}$  and  $10^{\circ}\text{N}$ . These upwelling and downwelling are due to waters going from the Central Indian basin onto the shallow Indonesian coast south of  $5^{\circ}\text{N}$ , and vice versa north of that latitude (see, again, [Fig. 8c](#)). In July, there is only one cell north of  $10^{\circ}\text{S}$  (not shown). It is clockwise and has a maximum strength of about 12 Sv near  $4^{\circ}\text{N}$ . The reason that there is only one cell is because the recirculating gyre in the Somali basin is much more dominant than that in the central Indian basin.

The vertical shear component ([Fig. 11d](#)) has the dominant seasonal variation south of  $25^{\circ}\text{S}$  and between  $5^{\circ}$  and  $8^{\circ}\text{N}$ . Examination of the zonal distribution of vertical shear indicates that 1) the fluctuation near the southern boundary is primarily due to changes of the model boundary currents, namely, the model Agulhas, East Madagascar, and Leeuwin Currents, and 2) that between  $5^{\circ}$  and  $8^{\circ}\text{N}$  is associated with change in the vertical shear of the Somali Current. The seasonal variation between  $25^{\circ}\text{S}$  and the equator is moderate (6 Sv) but larger than that of the external mode.

Since the decomposition is not meaningful near the equator for the reason mentioned earlier, we use the meridional velocity sections in [Fig. 9](#) to illustrate how the flows cross the equator; changes are mainly associated with the Somali Current and the corresponding shear flow reversal in the interior concentrated in the upper 200 m or so. Therefore, a more sensible description of flow variability near the equator is the variability of the barotropic gyre compensated by that of shear flows.

The relative contributions of various components for January (not shown) are similar to those for July, though not exactly symmetric. Therefore, Ekman flow together with a barotropic compensation is the dominant mechanism for seasonal variation in meridional overturning. The external mode together with bottom topography plays a secondary role. Vertical shear has a minor and major contribution north and south of  $25^{\circ}\text{S}$ , respectively.

## *b. Heat transport*

The total meridional heat transports for January, July, and the 12-month average are shown in [Fig. 12](#). The seasonal variations at most latitudes are larger than the annual averages, with a magnitude of up to  $\pm 1.8$  PW near  $10^{\circ}\text{S}$  and  $\pm 1.4$  PW near  $10^{\circ}\text{N}$ . Cross-equatorial heat transport varies by about  $\pm 0.9$  PW between January and July around an annual average of 0.4 PW. The only latitude band at which heat transport does not change sign from January to July is that south of  $17^{\circ}\text{S}$ . The heat transports presented in the figure are basically due to advective heat transport as the diffusive contribution is very small.

To examine the relative contributions of various dynamical components of meridional velocity in meridional heat transport, the total advective heat transport is decomposed into contributions by the external mode, Ekman component, and vertical shear by substituting the three components of the meridional velocity  $\mathbf{U}$  discussed in [section 3a](#) into  $\langle \mathbf{U} \nabla T \rangle$  (where  $T$  is temperature and  $\langle \rangle$  denotes zonal and  $[\ ]$  vertical integration). One can think of the three contributions to the advective heat transport as different meridional velocity fields (i.e., external mode, Ekman, and shear components) advecting the same temperature field. The external-mode, Ekman, and vertical-shear contributions to heat transport defined herein are exactly equivalent to the “barotropic,” “Ekman,” and “baroclinic” components of heat transport defined by [Hall and Bryden \(1982\)](#). However, we apply the decomposition to the meridional transport streamfunction as well as heat transport, and thus are able to examine the relative importance of these dynamical components in causing seasonal variation of the meridional overturning. We have also calculated the components of the heat transport due to the meridional overturning, which result from correlating the component streamfunctions in [Fig. 11](#) with the zonally averaged (rather than local) temperatures. The differences with [Fig. 13](#) presented below are minor, however.

The heat transport anomaly for July together with the three components are presented in [Fig. 13](#). The contribution of the Ekman component dominates except south of  $20^{\circ}\text{S}$ . Near the southern boundary, the vertical shear has the largest contribution, and is counteracted by the Ekman component and external mode. Its seasonal variation increases from  $25^{\circ}\text{S}$

toward the southern boundary. This variation is largely due to fluctuation in vertical shear associated with model boundary currents as mentioned in [section 3a](#). That of the external mode is relatively large near 5°N due to the gyre associated with the Somali Current. Farther north, the vertical shear contribution is larger than that of the external mode. In particular, the peak near 7°N is due to the large shear associated with the Somali Current. Note that the contribution from the Ekman component is stronger near 10°N than at 10°S, consistent with the variation in the Ekman component of the overturning. However, it is opposed by contributions from the external mode and vertical shear, leading to smaller total variation of heat transport at 10°N than at 10°S. The January decomposition is similar but with the reverse sign so it will not be presented.

One way the ocean affects the climate is by receiving heat in one location, transporting it to another location and then releasing it back to the atmosphere. Yet not all the heat being transported is released back to the atmosphere; a portion of it goes into storage. To illustrate the dominant mechanism controlling the transient heat balance, the time-dependent heat equation is integrated over zonal planes. [Figure 14](#) shows the resultant time rate of change of heat content (i.e., heat storage), (advective and diffusive) heat transport convergence, and surface heat flux as a function of time and latitude (contribution of heat by sponge layers has been included in the heat transport convergence). Since these quantities are calculated from model outputs using a time-differencing scheme that is slightly different from the GFDL model, the three terms sum up to very small residuals ( $\pm 3.5 \text{ W m}^{-2}$  rms about a mean of  $1.5 \text{ W m}^{-2}$ ) rather than to zero exactly. However, the residuals do not affect the following discussion.

In the northern and equatorial Indian Ocean (north of about 15°S), the dominant balance is between heat storage change and heat transport convergence because temporal variations of these two are large compared with that of heat exchange with the atmosphere, and they tend to compensate for each other. Therefore, if one considers the whole zonal plane of water as a parcel, the northern and equatorial Indian Ocean is relatively adiabatic. It implies that the dramatic monsoon reversal has little effect on heat exchange between the northern Indian Ocean and the atmosphere. South of 15°S, the three terms have comparable magnitudes, with the balance between heat transport convergence and surface heat flux being somewhat more prominent. Thus, the very southern part of the Indian Ocean is more diabatic in nature. These dominant balances on seasonal timescale are different from that of midlatitude World Ocean (away from land boundaries), where the heat storage change is thought to be primarily balanced by surface heat flux ([Gill and Niiler 1973](#)).

### *c. Rectification*

The 12-month average of the estimated meridional transport streamfunctions is presented in [Fig. 15](#) together with that resulting from the annual mean inversion (LM). Although the seasonal cycle in meridional overturning is large, the annual average streamfunction is very similar to that using annual mean data and forcings. This can be understood in terms of the dominant mechanisms responsible for the seasonal variation in meridional overturning, the Ekman flow, and the barotropic compensation. Since the compensation is achieved through barotropic waves, the adjustment to seasonally varying wind is relatively linear and so nonlinear rectification is small.

Sensitivity experiments with dramatically different initial states (in terms of overturning strength and direction) performed by LM indicates that final estimates of deep inflow strength ranges from 2 to 10 Sv. Within this range, the larger the deep inflow strength, the more unrealistic the throughflow structure becomes. Therefore, only an inflow of a few Sverdrups is considered to be a consistent solution. Note that one should not interpret the streamfunctions presented in [Fig. 15](#) as having no deep inflow at all.

The small amount of estimated northward deep inflow into the Indian Ocean is similar to the findings from the geostrophic calculation by [Toole and Raymer \(1985\)](#), the regional linear inversion by [Fu \(1986\)](#), and the high-resolution global and regional GCM simulations of [Semtner and Chervin \(1992\)](#) and [Wacongne and Pacanowski \(1996\)](#), all within a few Sverdrups. It is smaller than those estimated by the global and regional linear inversions of [Macdonald \(1995\)](#) and [Robbins and Toole \(1997\)](#), both around 10 Sv, and much smaller than the 27 Sv obtained from the geostrophic calculation by [Toole and Warren \(1993\)](#). While GCMs are hampered by inadequate data constraints and model errors, geostrophic calculations and linear inversions have potential bias in the choice of the levels of no motion (LMN). The extremely large transport reported by Toole and Warren has been revised by Robbins and Toole by using a silica budget as an additional constraint to the choice of LMN.

As discussed in LM, the weak estimate of northward deep inflow might be due to model errors, one of which being the absence of a net mass flux resulting from the crude open boundary conditions (sponge layer). The low resolution of the model together with the smoothed Levitus data may also contribute. The deep inflows are carried northward by deep western boundary currents (DWBCs) in different basins ([Toole and Warren 1993](#)). Our estimated annual mean meridional velocity section near the southern boundary (27.25°S) ([Fig. 16](#)) shows well-defined DWBCs pressing against the western side of the Mozambique Channel, the Madagascar Ridge, and the Central Indian Ridge (that against the Ninety East Ridge is missing). The annual mean signatures of DWBCs are very similar to those estimated from an assimilation with annual mean data and forcings presented by LM, indicating a lack of seasonal rectification to the deep currents. The estimated DWBCs are much broader and weaker than those calculated by Toole and Warren. The high-resolution GCM of



Semtner and Chervin shows narrower DWBC than our model, but still yields a small northward net inflow probably because of the compensation by horizontal return flow.

The 12-month averaged meridional heat transport is presented in [Fig. 17](#) together with the heat transport estimate resulting from the annual mean experiment (thick and thin solid curves, respectively). The two are similar, with about 0.1 PW offset in the southern Indian Ocean, and less in the northern Indian Ocean. Therefore, the rectification of seasonal forcings to the annual mean heat transport is also small. This, however, is not true for the heat transport due to the time-mean fields of meridional velocity and temperature. To illustrate this, the meridional velocity and temperature fields are decomposed into time-mean and time-varying fields:  $\mathbf{v} = \langle \mathbf{v} \rangle + \mathbf{v}'$  and  $T = \langle T \rangle + T'$ , where angle brackets denote time average. The 12-month averaged heat transport can then be decomposed into two components  $\langle \mathbf{v}T \rangle = \langle \mathbf{v} \rangle \langle T \rangle + \langle \mathbf{v}'T' \rangle$ . The two terms correspond to contributions from the time-mean circulation and temperature fields and from the correlation of time-varying velocity and temperature fields, which are presented as the dashed and dashed-dotted curves in [Fig. 17](#). In the northern Indian Ocean, these two contributions are comparable, reflecting a significant seasonal rectification in heat transport. The lower heat transport of the time-mean part for the northern Indian Ocean is largely because of the lower SST with seasonal forcings than without, which is an improvement of the optimization as mentioned earlier.

To illustrate dominant processes controlling time-mean and time-varying parts of the annual-averaged heat transport, the time-mean and time-varying fields of meridional velocities and temperatures are decomposed into horizontal averages and deviation from them. The time-mean and time-varying components of the heat transport can then be partitioned into the so-called “overturning” and “horizontal gyre” contributions (after [Hall and Bryden 1982](#)). The results are presented in [Fig. 18](#) (dashed and dashed-dotted curves). While the time-mean contribution to heat transport is largely due to the meridional overturning ([Fig. 18a](#)), the time-correlation part is primarily contributed by the horizontal gyre ([Fig. 18b](#)). The latter is associated with the reversal of the Somali Current and the corresponding horizontal circulation. Note that the gyre transports heat southward north of  $10^\circ\text{N}$  ([Fig. 18a](#)), counteracting the northward heat transport by the overturning. The combined effect results in small ( $<0.05$  PW) northward total heat transports close to the northern boundary. This may be due to the underestimated strength of the horizontal gyre there or due to the relatively wide northern sponge used to represent effect of the narrow connection to the Persian Gulf.

#### *d. Comparison with other studies*

[Wacongne and Pacanowski \(1996\)](#) presented the meridional streamfunction north of  $15^\circ\text{S}$  for the months of February and August. [Garternicht and Schott \(1997\)](#) showed the same function north of  $10^\circ$  for January and July. A common feature in seasonal variations of the overturning among our estimate and these two studies is that the variation is large both in magnitude (roughly  $\pm 20$  Sv) and depth of penetration (top to bottom). However, the overturning streamfunctions near the peaks of the two monsoon seasons appear to be more symmetric about the annual average in our study and that of GS97 than in Wacongne and Pacanowski. There are other differences in detail of the overturning for the three studies as well. For instance, the seasonally reversing cell near  $10^\circ\text{N}$  in our estimated streamfunction is not seen in the other two studies.

The gross resemblance in seasonal overturnings result in similar seasonal variations in meridional heat transport: approximately  $\pm 1$  PW at the equator for all three studies. The variation at  $10^\circ\text{N}$  is about  $\pm 1.4$  PW in our study,  $\pm 1.2$  PW in GS97, and  $\pm 1$  PW in Wacongne and Pacanowski. In comparison, the heat transport variation reported by [McCreary et al. \(1993\)](#) using a 2½-layer model is smaller primarily because of the absence of the intermediate and deep overturning.

Our dynamical decomposition of the overturning and heat transport shows that seasonal variation in Ekman flow (caused by change in zonal wind stress) together with a barotropic compensation is the major contributor to seasonal heat transport. This is consistent with the strong linear relation between zonal wind stress and heat transport reported by GS97.

The dominant annual average overturning is very shallow (in the upper 500 m north of  $10^\circ\text{S}$ ) in all three studies. However, in our experiments the strength of this dominant overturning is somewhat larger, and its base (i.e., the depth of the zero-transport streamline) is slightly deeper. Consequently, our estimated annual average southward heat transport is larger north of  $10^\circ\text{S}$ . GS97 reported that the contribution of the horizontal gyre north of the equator to heat transport is larger than that of the overturning. The opposite is true in our study except north of  $8^\circ\text{N}$ .

We assume that differences between the wind products [estimated wind in this study using Hellerman and Rosenstein wind as prior estimates, ECMWF wind during 1987–89 in GS97, and Comprehensive Ocean–Atmosphere Data Set wind in Wacongne and Pacanowski] is one major cause for differences in the overturning and heat transport. In particular, the very weak annual average overturning reported by GS97 north of the equator may be a result of the weak ECMWF zonal wind stress, which also weakens the contribution of the overturning in transporting heat as compared with that due to the horizontal gyre. However, differences might be caused by different grid resolutions, differences in surface heat and freshwater flux formulation (estimated flux in this study and relaxation in the other two studies), and differences in side-boundary conditions (estimation of sponge layer properties in this study, imposed sponge layer properties in Wacongne and Pacanowski, and open boundaries in GS97).

Our zonally integrated seasonal surface heat flux estimates are in fairly good agreement with the climatological data of [Hastenrath and Greischar \(1993\)](#) both in terms of the phase and magnitude. The annual averaged meridional heat transport from our study is compared with those simulated by [Wacongne and Pacanowski \(1996\)](#) and GS97 using regional and global GCMs and that inferred from climatological heat flux data by [Hastenrath and Greischar \(1993\)](#) ([Fig. 19](#)). Our estimated southward heat transports are in relatively good agreement with those of Hastenrath and Greischar, and are generally larger than those simulated by the two GCMs except south of 15°S in GS97 (dotted curve) because of a significant enhancement of temperature flux by the throughflow.

Despite significant regional differences, there are strong dynamical similarities between the seasonal cycles in mass and heat transports described here and those of the high-resolution North Atlantic model analyzed by [Böning and Herrmann \(1994\)](#). The latter found seasonally reversing meridional overturning roughly between 5°S and 20°N and weaker seasonal variability farther north. In the North Atlantic, seasonal reversal of the zonal wind occurs only in narrow latitude bands, so the Ekman transport mostly does not reverse sign. However, [Böning and Herrmann \(1994\)](#) also found that the seasonal Ekman transport anomalies are compensated largely by barotropic flow. They did not perform a formal dynamical decomposition of the meridional overturning analogous to our [Fig. 11](#), so it is not entirely clear why their equatorial overturning reversed direction although the wind stress did not. However, the seasonal disappearance and reappearance of the North Equatorial Countercurrent suggests an effect akin to that of the seasonal reversal of the Somali current: the external mode shows a very strong seasonal signal, which in the presence of topography (e.g., northward flow over shallow topography, southward flow over deep) projects onto the meridional overturning (generally in a depth-dependent way). [Böning and Herrmann \(1994\)](#) also noticed that Ekman transport fluctuations were largely responsible for the heat transport variability, and that in the equatorial Atlantic heat transport variations were balanced by storage changes. Overall, the seasonal transport variability seems to be made of the same dynamical “building blocks” in the two models, although the relative strengths clearly are different.

#### 4. Inclusion of TOPEX data

The optimization with hydrographic data is extended by introducing TOPEX-derived surface geostrophic velocity anomalies as additional constraints. After 50 iterations (beyond the 80 iterations of the previous experiment), the model–data misfit due to the penalty of the TOPEX data decreases by approximately two-thirds to an overall acceptable level. The deviations of  $T$  and  $S$  from Levitus data only decrease slightly.

The resultant meridional streamfunctions for January and July are shown in [Fig. 20](#) together with their counterparts obtained from the hydrography-only experiment. The seasonal variation of the overturning is enhanced by the inclusion of TOPEX data, especially near the Indonesian Throughflow latitudes (20°–7°S). The same comparison for meridional heat transport ([Fig. 21](#)) indicates that seasonal variation in heat transport in the central Indian Ocean is enhanced by roughly 0.5 PW. By decomposing the overturning and heat transport into various dynamical components as described in [section 3a](#), it is found that these changes are primarily due to changes in the Ekman component (associated with changes in estimated zonal wind stress) and the thermal wind shear near the throughflow region (not shown).

The inclusion of TOPEX data also improved the estimated zonal flows near the equator. An example is the behavior of the eastward EUC near 55°E ([Fig. 22](#)): it begins emerging in January near the equator and is centered between 50 and 100 m, shifting southward in February through April, and merging with the eastward ECC farther south in May. The zonal velocity core of the model EUC is broader (in the vertical–meridional plane) than in the observations, and the maximum strength (20–25 cm s<sup>-1</sup> in April) is several times smaller than observed by [Leetmaa and Stommel \(1980\)](#). This is not surprising given the limited vertical and horizontal resolution and mixing formulation. Since the TOPEX-derived geostrophic velocities within ±2.5° of the equator were excluded from the assimilation ([section 2](#)), the information contained in the TOPEX data outside this latitude band must be propagated to within the band through model dynamics to affect the behavior of the EUC. Another example of improved equatorial zonal flows is that the amplitude of the semiannual oscillations in subsurface equatorial zonal flow (discussed in [section 3](#)) increases by 25%, making it somewhat closer to observations ([Luyten and Roemmich 1982](#)).

Apart from the impact on the estimated meridional overturning and heat transport and the improved estimates of equatorial zonal flows, the assimilation of TOPEX data also results in more realistic large-scale and regional features such as the thermocline variation in the southern Indian Ocean. They will be presented elsewhere as the focus of this paper is the overturning and heat transport.

[Figure 23](#) shows the vertical profiles of meridionally averaged zonal velocity at the edge of the throughflow sponge for January and July for the hydrography-only and hydrography plus TOPEX experiments. With TOPEX data, the baroclinic mass exchange between the model interior and the throughflow sponge becomes larger, especially in July. TOPEX data require a large inflow from the throughflow sponge into the interior near the surface. However, the estimated vertical shear is large even at depths. The integrated transport below 2000 m is approximately 13 Sv (into the sponge). Although observations of the velocity structure near the throughflow region are limited, all velocity profiles documented in previous

literature (e.g., [Fieux et al. 1996](#), [Meyers 1996](#)) indicate that much of the flow into the interior is concentrated in the top few hundred meters and there is little vertical shear at depth. Therefore, the July profile of zonal velocity after TOPEX data are assimilated is inconsistent with velocity observations near the throughflow region. The large vertical shear is supported by a large meridional density gradient (through thermal wind), resulting in meridional temperature gradients near the edge of the throughflow sponge that are much larger than those estimated without TOPEX data.

One possible cause for this inconsistency is the absence of formal open boundary conditions in the model, which would allow shallow flow from the throughflow into the model interior without demanding mass compensation. For a sponge layer, however, an equal amount of flow has to return to the sponge layer, resulting in an unrealistic vertical profile of velocity. The artificial return flow requires meridional temperature gradients to support it, leading to large deviations in density structure from Levitus data.

The inconsistency might also arise because the Levitus climatology, which is compiled from hydrographic data spanning many decades, is incompatible with the 3-yr-averaged seasonal anomalies of TOPEX data. Even within the 3-yr period of TOPEX data there is large interannual variability near the throughflow region. Therefore, if one excludes this variability, the inconsistency between Levitus and TOPEX data near the throughflow area is not surprising. When interannual variability is included as data error, the solution derived from the hydrography-only experiment is already consistent with the TOPEX data. The reason for excluding the interannual “error” was to test the impact of TOPEX data on the model solution.

## 5. Concluding remarks

A GCM of the Indian Ocean is fitted to monthly averaged climatological temperatures, salinities, and surface fluxes using the adjoint method. Interannual variability is minimized by penalizing the temporal drift from one seasonal cycle to another during a two-year integration. Monthly properties in sponge layers near the southern boundary, the Indonesian Throughflow channel, the Red Sea, and the Persian Gulf are estimated as part of the optimization procedure. A steady seasonal cycle of the GCM is found that is consistent with the climatological data within limits of observational uncertainties. The estimated SST are closer to the climatological values with seasonal forcings than without.

The resultant meridional overturning displays large seasonal variation: it reverses over the full depth of the model ocean at the peaks of the two monsoon seasons; the largest variations occur near 10°S and 10°N ( $\pm 18$  and  $\pm 22$  Sv, respectively), which correspond to the latitudes where the easterlies over the southern Indian Ocean and the monsoon over the northern Indian Ocean have the largest seasonal variability. Consequently, seasonal variation in meridional heat transport is strong (1.8 and 1.4 PW, respectively).

The meridional transport streamfunction is decomposed into three components to highlight the relative importance of various dynamical processes in causing the seasonal cycles: the external mode plus zonally varying topography, the Ekman flow plus a barotropic compensation, and vertically sheared flow comprising thermal wind and ageostrophic flow associated with friction and nonlinear effects. Overall, the Ekman component causes dominant seasonal variations in meridional overturning and heat transport due to monsoon reversal over the northern Indian Ocean and the change of easterlies over the subtropical southern Indian Ocean. The external mode causes moderate seasonal variations at latitudes where the Somali Current and the corresponding gyre reverse direction seasonally. Thermal wind and ageostrophic shear have dominant contributions near the southern boundary and the equator. While GS97 found an empirical linear relation between zonal wind stress and meridional heat transport, our decomposition of the overturning and heat transport provides a dynamical interpretation of the relative contributions from various processes, with the Ekman flow plus a barotropic compensation being the dominant one.

While seasonal variation in meridional overturning is large, seasonal forcings cause little rectification in the annual average overturning, probably because of the linearity of the dominant mechanism controlling the overturning variation. The annual average meridional heat transport is also similar to that derived from the optimization using annual mean forcings. The heat transport is further decomposed into contributions due to time-mean meridional velocities and temperatures and due to the time-correlation of the time-varying meridional velocities and temperatures. In the southern Indian Ocean, the contribution is primarily due to the time-mean fields. In the northern Indian Ocean, however, contributions from the time-mean and time-varying fields have comparable magnitudes, indicating a significant seasonal rectification in the time-mean SST and heat transport. While the time-mean contribution is primarily due to the overturning, the time-varying field contribution is associated with the horizontal gyre (as a result of the Somali Current reversal).

The dominant balance in the heat budget is between the time rate of change of heat content and meridional heat transport convergence except south of about 15°S. In other words, the northern Indian Ocean as a whole is more adiabatic as compared with the very southern part of the Indian Ocean. This is in contrast to the midlatitude ocean, which is relatively more diabatic (heat storage change primarily balanced by surface heat flux).

Our estimated seasonal cycles of overturning and heat transport are in qualitative agreement with those reported by

Wacongne and Pacanowski (1996) derived from a high-resolution GCM of the Indian Ocean north of 15°S, and by GS97 obtained from the Indian Ocean sector (north of 10°S) of a global high-resolution GCM simulation. However, our estimated annual average meridional heat transports are generally stronger than those in these two studies, and are in good agreement with those inferred from climatological heat flux data by Hastenrath and Greischar (1993).

Inclusion of TOPEX-derived surface geostrophic velocity anomalies as additional constraints enhances the seasonal cycles of the meridional overturning and heat transport in the central Indian Ocean and improves the estimated equatorial zonal flows, but leads to velocity structure near the Indonesian Throughflow region that is inconsistent with observations. This might partly be due to the lack of a barotropic component of the throughflow, and partly because of the large interannual variability of the throughflow captured by TOPEX during a 3-yr period (1992–95). The experience with TOPEX data assimilation suggests that one should incorporate open boundaries and allow interannual variability in the assimilation to use TOPEX data more effectively.

The meridional velocities associated with the barotropic compensation to the Ekman flow are too weak to be measured (order of 0.01–0.1 cm s<sup>-1</sup>). Therefore, it would be very difficult to confirm directly whether this dominant mechanism that controls the model meridional overturning and heat transport is indeed at work in the real Indian Ocean on seasonal timescale. However, one can examine whether the measured Ekman flow of the Indian Ocean is approximately compensated by shallow shear flows. If it is, the dominant mechanism shown in this study would be an artifact. Otherwise, the seasonal (and interannual for that matter) heat transport of the Indian Ocean can be inferred reasonably well from accurate observations of zonal wind stress and wind stress curl (e.g., scatterometer measurements). Hydrographic measurements can be used to estimate the remaining contribution to the transient heat transport, which is primarily associated with thermal wind shear.

### Acknowledgments

This work was supported by grant OCE-930135 from the National Science Foundation. The computations were performed on Cray-YMPs at the National Center for Environmental Prediction and the National Center for Atmospheric Research, which is supported by the National Science Foundation. Special thanks are due to Dr. Detlef Stammer for providing us with 2° maps of sea surface heights of the Indian Ocean.

---

### REFERENCES

- Anderson, D. L. T., and D. J. Carrington, 1993: Modeling interannual variability in the Indian Ocean using momentum fluxes from the operational weather analyses of the United Kingdom Meteorological Office and European Centre for Medium-Range Weather Forecasts. *J. Geophys. Res.*, **98**, 12 483–12 499.
- Böning, C. W., and P. Herrmann, 1994: Annual cycle of poleward heat transport in the ocean: Results from high-resolution modelling of the North and equatorial Atlantic. *J. Phys. Oceanogr.*, **24**, 91–107.
- Cox, M. D., 1984: A primitive equation, 3-dimensional model of the ocean. GFDL Ocean Group Tech. Rep. No. 1, Geophysical Fluid Dynamics Laboratory, Princeton University, Princeton, NJ.
- Fieux, M., R. Molcard, and A. G. Ilahude, 1996: Geostrophic transport of the Pacific–Indian Oceans throughflow. *J. Geophys. Res.*, **101**, 12 421–12 432.
- Fu, L.-L., 1986: Mass, heat, and freshwater fluxes in the South Indian Ocean. *J. Phys. Oceanogr.*, **16**, 1683–1693.
- Garnier, U., and F. Schott, 1997: Heat fluxes of the Indian Ocean from a global eddy-resolving model. *J. Geophys. Res.*, in press.
- Gill, A. E., and P. P. Niler, 1973: The theory of the seasonal variability in the ocean. *Deep-Sea Res.*, **20**, 141–147.
- Hall, M. M., and H. L. Bryden, 1982: Direct estimates and mechanisms of ocean heat transport. *Deep-Sea Res.*, **29**, 339–360.
- Hastenrath, S., and L. Greischar, 1993: The monsoonal heat budget of the hydrosphere–atmosphere system in the Indian Ocean sector. *J. Geophys. Res.*, **98**, 6869–6881.
- Hellerman, S., and M. Rosenstein, 1983: Normal monthly wind stress over the World Ocean with error estimates. *J. Phys. Oceanogr.*, **13**, 1093–1104.
- Latif, M., A. Sterl, M. Assenbaum, M. M. Junge, and E. Maier-Reimer, 1994: Climate variability in a coupled GCM. Part II: The Indian Ocean. *J. Climate*, **7**, 1449–1462. [Find this article online](#)



- Lee, T., and J. Marotzke, 1997: Inferring meridional mass and heat transports of the Indian Ocean by fitting a general circulation model to climatological data. *J. Geophys. Res.*, **102**, 10 585–10 602..
- Leetmaa, A., and H. Stommel, 1980: Equatorial current observations in the western Indian Ocean in 1975 and 1976. *J. Phys. Oceanogr.*, **10**, 258–269..
- Levitus, S., 1982: *Climatological Atlas of the World Ocean*. NOAA Prof. Paper No. 13, U.S. Govt. Printing Office, 173 pp..
- , and T. P. Boyer, 1994: *World Ocean Atlas 1994*. Vol. 4: *Temperature*. NOAA Atlas NESDIS 4, U.S. Department of Commerce, NOAA, NESDIS, 117 pp..
- , R. Burgett, and T. P. Boyer, 1994: *World Ocean Atlas 1994*. Vol. 3: *Salinity*. NOAA Atlas NESDIS 3, U.S. Department of Commerce, NOAA, NESDIS, 99 pp..
- Luyten, J. R., and D. H. Roemmich, 1982: Equatorial currents at semi-annual period in the Indian Ocean. *J. Phys. Oceanogr.*, **12**, 406–413..
- Macdonald, A., 1995: Oceanic fluxes of mass, heat, and freshwater: A global estimate and perspective. Ph.D dissertation, Massachusetts Institute of Technology, 326 pp..
- Marotzke, J., 1992: The role of integration time in determining a steady state through data assimilation. *J. Phys. Oceanogr.*, **22**, 1556–1567..
- , 1997: Boundary mixing and the dynamics of three-dimensional thermohaline circulations. *J. Phys. Oceanogr.*, **27**, 1713–1728..
- McCreary, J. P., Jr., P. K. Kundu, and R. L. Molinari, 1993: A numerical investigation of dynamics, thermodynamics and mixed-layer processes in the Indian Ocean. *Progress in Oceanography*, Vol. 31, Pergamon, 181–244..
- Meyers, G., 1996: Variation of Indonesian Throughflow and the El Niño–Southern Oscillation. *J. Geophys. Res.*, **101**, 12 255–12 263..
- Oberhuber, J. M., 1988: *An Atlas Based on the COADS Data Set: The Budgets of Heat, Buoyancy and Turbulent Kinetic Energy at the Surface of the Global Ocean*. Max-Planck-Institut für Meteorologie, 100 pp..
- Robbins, P. E., and J. M. Toole, 1997: The dissolved silica budget as a constraint on the meridional overturning circulation of the Indian Ocean. *Deep-Sea Res.*, **44**, 879–906..
- Schott, F., J. Swallow, and M. Fieux, 1989: Deep currents underneath the equatorial Somali current. *Deep-Sea Res.*, **36**, 1191–1199..
- , —, and —, 1990: The Somali Current at the equator: Annual cycle of currents and transports in the upper 1000 m and connection to neighboring latitudes. *Deep-Sea Res.*, **37**, 1825–1848..
- , J. Reppin, and J. Fisher, 1994: Currents and transports of the monsoon current south of Sri Lanka. *J. Geophys. Res.*, **99**, 25 127–25 141..
- Semtner, A. J., Jr., and R. M. Chervin, 1992: Ocean general circulation from a global eddy-resolving model. *J. Geophys. Res.*, **97**, 5493–5550..
- Thacker, W. C., and R. B. Long, 1988: Fitting dynamics to data. *J. Geophys. Res.*, **93**, 1227–1240..
- Toole, J. M., and M. E. Raymer, 1985: Heat and fresh water budgets of the Indian Ocean revisited. *Deep-Sea Res.*, **32**, 917–928..
- , and B. A. Warren, 1993: A hydrographic section across the subtropical South Indian Ocean. *Deep-Sea Res.*, **40**, 1973–2019..
- Wacongne, S., and R. Pacanowski, 1996: Seasonal heat transport in a primitive equations model of the tropical Indian Ocean. *J. Phys. Oceanogr.*, **26**, 2666–2699..
- Warren, B. A., and G. C. Johnson, 1992: Deep currents in the Arabian Sea in 1987. *Mar. Geol.*, **104**, 279–288..
- Wyrtki, K., 1973: An equatorial jet in the Indian Ocean. *Science*, **181**, 262–264..

---

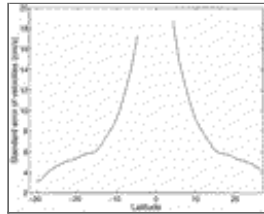
## Tables

Table 1. Prescribed standard errors of monthly  $T$  and  $S$ ,  $\delta_t$  and  $\delta_s$ , for various depths.

Depth (m)	$\delta_t$ (°C)	$\delta_s$ (psu)
12.5	1.54	0.22
37.5	1.51	0.21
62.5	1.48	0.21
87.5	1.43	0.20
125.0	1.35	0.19
200.0	1.20	0.18
300.0	1.13	0.16
400.0	1.11	0.16
500.0	1.07	0.14
600.0	0.96	0.12
700.0	0.84	0.11
850.0	0.70	0.09
1050.0	0.57	0.08
1250.0	0.44	0.07
1500.0	0.32	0.06
1850.0	0.20	0.04
2300.0	0.11	0.02
2800.0	0.06	0.01
3300.0	0.04	0.01
3800.0	0.04	0.01
4300.0	0.04	0.01
4800.0	0.04	0.01
5300.0	0.03	0.01
5800.0	0.01	0.01

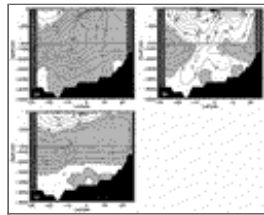
[Click on thumbnail for full-sized image.](#)

## Figures



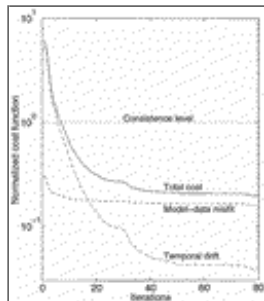
[Click on thumbnail for full-sized image.](#)

Fig. 1. Zonally averaged standard errors of surface geostrophic velocity anomalies derived from TOPEX data for the period of 1993–95.



[Click on thumbnail for full-sized image.](#)

Fig. 2. Meridional transport streamfunction for January (a), July (b), and annual average (c) resulting from 100 years of forward integration. Contour interval is 4 Sv. Positive and negative contours indicate general clockwise and counterclockwise overturning, respectively.



[Click on thumbnail for full-sized image.](#)

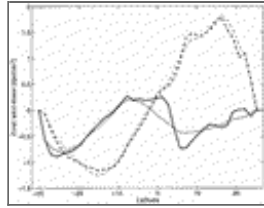
Fig. 3. Normalized cost function and its two components, model–data misfit and temporal drift, as a function of iteration.





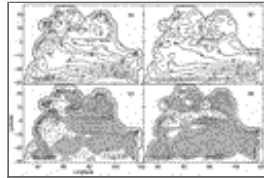
[Click on thumbnail for full-sized image.](#)

Fig. 4. Hellerman–Rosenstein wind stress for (a) January and (b) July, the corresponding estimates of wind stress (c) and (d), and their differences (e) and (f).



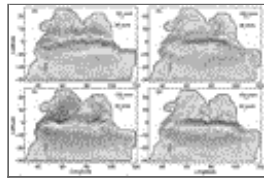
[Click on thumbnail for full-sized image.](#)

Fig. 5. Zonally averaged zonal wind stress for January (solid curves) and July (dashed curves). The thin and thick curves correspond to the prior and estimated winds.



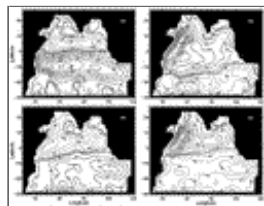
[Click on thumbnail for full-sized image.](#)

Fig. 6. Estimated SST with annual mean forcings (a) and annual average of estimated SST with seasonal forcings (b). The corresponding deviations from Levitus data are shown in (c) and (d) (positive values indicate warmer estimates).



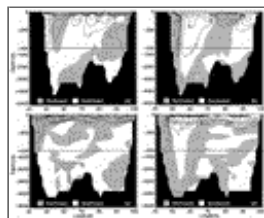
[Click on thumbnail for full-sized image.](#)

Fig. 7. Estimated surface currents for January (a), April (b), July (c), and October (d). Arrow lengths proportional to the square roots of velocity.



[Click on thumbnail for full-sized image.](#)

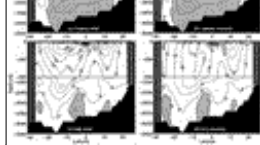
Fig. 8. Estimated barotropic streamfunctions for January and July (a) and (b) and their corresponding seasonal anomalies (c) and (d). Contour levels are in Sverdrups.



[Click on thumbnail for full-sized image.](#)

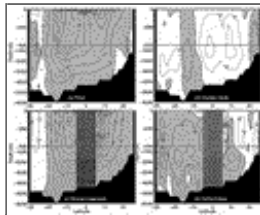
Fig. 9. Meridional velocity sections for January and July at 5.75°N (a) and (b) and 0.25°S (c) and (d). Contour levels in centimeter per second.





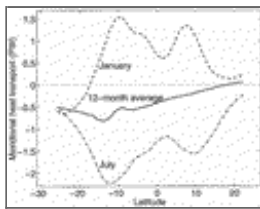
[Click on thumbnail for full-sized image.](#)

Fig. 10. Meridional transport streamfunctions for January and July (left) and their seasonal anomalies (right) (contour levels in Sv).



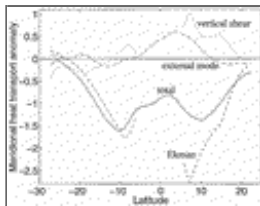
[Click on thumbnail for full-sized image.](#)

Fig. 11. Decomposition of meridional transport streamfunction anomaly in January (a) into contributions from the external mode (b), the Ekman component (c), and vertical shear (d).



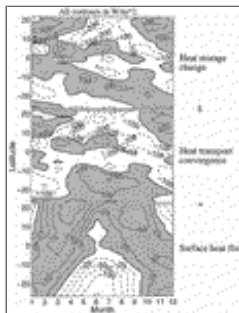
[Click on thumbnail for full-sized image.](#)

Fig. 12. Meridional heat transports for January, July, and 12-month average.



[Click on thumbnail for full-sized image.](#)

Fig. 13. Decomposition of total heat transport anomaly (solid) into the external mode (dash-dotted), Ekman (dashed), and vertical shear (dotted) components (July example).



[Click on thumbnail for full-sized image.](#)

Fig. 14. Zonally and vertically integrated heat budget as a function of time and latitude.

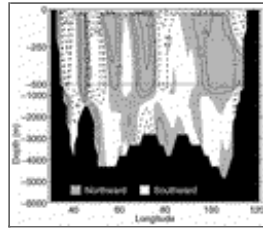






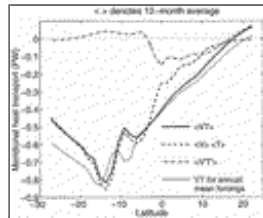
Click on thumbnail for full-sized image.

Fig. 15. Meridional streamfunction obtained from 12-month average of seasonal estimates (a) and that resulting from annual mean forcing experiment (b).



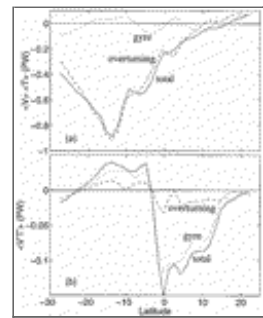
Click on thumbnail for full-sized image.

Fig. 16. Annual mean meridional velocity section near the southern boundary (27.25°S). Northward-flowing deep western boundary currents are seen pressing against the western side of the Mazambique Channel, the Madagascar Ridge, and the Central Indian Ridge.



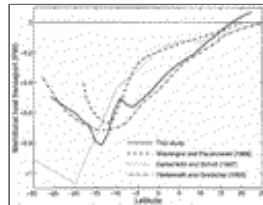
Click on thumbnail for full-sized image.

Fig. 17. Rectification of meridional heat transport by seasonal forcings. Thick solid curve represents 12-month averaged total advective heat transport; dashed curve indicates the contribution of the 12-month-averaged meridional velocities and 12-month-averaged temperatures; dash-dotted curve denotes the contribution from the correlation of time-varying meridional velocities and temperatures; thin solid curve corresponds to heat transport resulting from the annual mean forcing experiment.



Click on thumbnail for full-sized image.

Fig. 18. Decomposition of total heat transports due to time-mean (a) and time-varying (b) fields into overturning and gyre components.



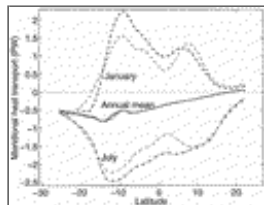
Click on thumbnail for full-sized image.

Fig. 19. Comparison of estimated annual average of heat transport with other studies.



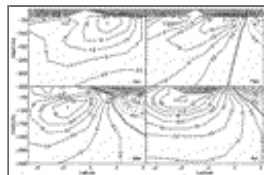
 Click on thumbnail for full-sized image.

Fig. 20. Meridional streamfunctions resulting from optimizations with hydrography only (a) and (b) and with hydrography plus TOPEX data (c) and (d).



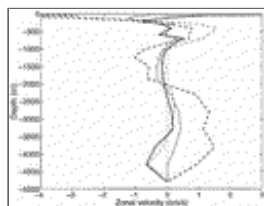
Click on thumbnail for full-sized image.

Fig. 21. Estimated meridional heat transport for January, July, and annual average. Gray and black curves correspond to estimates from the hydrography-only and hydrography plus TOPEX data experiments, respectively.



Click on thumbnail for full-sized image.

Fig. 22. Meridional section of zonal velocity at 55.25°E and near the equator (with TOPEX data assimilated). The undercurrent core shifts southward from January to April and merges with the countercurrent in May, which compares reasonably well with [Leetmaa and Stommel \(1980\)](#)



Click on thumbnail for full-sized image.

Fig. 23. Vertical profiles of meridionally averaged zonal velocity for January (solid) and July (dashed) across the throughflow sponge. Thin and thick curves correspond to estimates from the hydrography-only and hydrography plus TOPEX data experiments.

Corresponding author address: Dr. Tong Lee, Jet Propulsion Laboratory, MS 300-323, 4800 Oak Grove Dr., Pasadena, CA 91109.

E-mail: [tlee@pacific.jpl.nasa.gov](mailto:tlee@pacific.jpl.nasa.gov)

top ▲



© 2008 American Meteorological Society [Privacy Policy and Disclaimer](#)  
Headquarters: 45 Beacon Street Boston, MA 02108-3693  
DC Office: 1120 G Street, NW, Suite 800 Washington DC, 20005-3826  
[amsinfo@ametsoc.org](mailto:amsinfo@ametsoc.org) Phone: 617-227-2425 Fax: 617-742-8718  
[Allen Press, Inc.](#) assists in the online publication of AMS journals.